Ultrathin graphene oxide encapsulated in uniform MIL-88A(Fe) for enhanced visible light-driven photodegradation of RhB

Ning Liu[a,1], Wenyuan Huang[a,1], Xiaodong Zhang[a,*], Liang Tang[b], Liang Wang[b], Yuxin Wang[c], Minghong Wu[b,*]

[a] School of Environment and Architecture, University of Shanghai for Science and technology, Shanghai 200093, China
[b] School of Environmental and Chemical Engineering, Shanghai University, Shanghai 200444, China
[c] Institute of Applied Biotechnology, Taizhou Vocation & Technical College, Taizhou Zhejiang 318000, China

ABSTRACT

It is very important to design excellent heterojunction structure for the improvement of the photocatalytic performance. In this study, we report a facile approach of polymerizing the ultrathin graphene oxide on the surface of the MIL-88A(Fe) to form MIL-88A(Fe)/grapheme oxide composite for enhancing the photocatalytic efficiency of organic molecules degradation. The optical grapheme oxide doping content in MIL-88A(Fe)/grapheme oxide hybrid is determined to be 9.0 wt% , which increases the surface area of the MOFs from 15.9 m^2g^{-1} to 408.9 m^2g^{-1} due to the emerging micropores, and the corresponding photocatalytic rate for RhB is 8.4 times higher than that of pure MIL-88A(Fe). Meanwhile, DMF-free MOF-based heterostructure could avoid secondary contamination in the photocatalytic application process, and the degree of RhB removal is maintained at about 100% after the five cycles of the reaction. Integrating the related electrochemical analysis and the active species trapping experiments, the decisive factors for the improved photocatalytic efficiency of MIL-88A(Fe)/grapheme oxide may be the unique structural advantages of ultrathin grapheme oxide sheets, compact and uniform interface contact, more adsorption sites and more reaction sites. This work provides a novel sight for preparing high-efficient and environment-stable photocatalysts by designing the surface heterojunction structure.

1. Introduction

Metal organic frameworks (MOFs), formed by polydentate organic linkers and metal ions or metal clusters, are a class of advanced crystalline composite porous materials [1–3]. Owing to their high surface area, well-distributed but adjustable pores and easily tailored chemical properties, MOFs have many outstanding performances and potential applications in drug delivery, gas storage, molecular sensing, separation and catalysis [4–9]. Recently, MOFs have been used for light harvesting because they possess chromophores that can interact with light and undergo photochemical process after photo-excitation [10]. For instance, a well-known MOF-5 reported by the group of Garcia has been demonstrated to be a distinguished photocatalyst for phenol removal under UV light irradiation [11]. A Cu-doped ZIF-67 has been applied as a photocatalyst for the decolorization of methyl orange under visible light [12]. Some Zr-based NH_2-UiO-66 MOFs have also displayed visible-light-driven photocatalysts for the degradation of organic pollutants and the reduction of Cr(VI) [13,14].
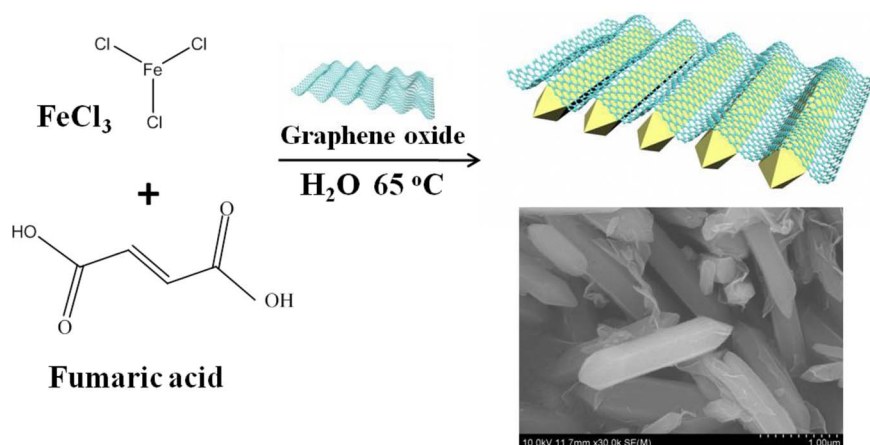
Of note, although some MOFs are capable of interacting with visible light in solar spectrum, the activities of those MOF photocatalysts are restricted by the relatively poor separation and migration of photogenerated electron-hole pairs. Up to now, many strategies have been used to improve the photocatalytic efficiencies of MOFs by inhibiting charge carriers recombination, such as surface modification and doping [15]. Among them, it is popular that the utilization of noble metal or metal oxide (such as Ag, Pt, Au, Pd) to improve the photocatalytic efficiency of MOFs by forming heterostructured photocatalysts [16,17], but the inevitable shortcomings of limited content and high price of noble metal constrain its practical application [17].

Alternatively, another feasible and significant strategy to enhance photogenerated charge carries separation and thus enlarge their lifetime is the combination semiconductor with graphene oxide (GO) to form heterojunctions, owing to the superior charge carrier mobility,

---

* Corresponding authors.
  E-mail addresses: zhangxiaodong@usst.edu.cn, fatzhxd@126.com (X. Zhang), mhwu@shu.edu.cn (M. Wu).
[1] These authors contributed equally to this work and should be considered as co-first authors.

high specific surface area, and high electrical conductivity of GO [18,19]. It has reported that the photocatalytic applications of several GO-semiconductor (e.g., TiO_2, ZnO, Bi_2WO_6, CdS, WO_3 and MOFs) and those composites could enhance the photoreactivity. MIL-53(Fe)-graphene nanocomposites are prepared as efficient visible-light photocatalysts for the selective oxidation of alcohols [20]. A novel MIL-68(In)-NH_2/graphene oxide composite is prepared as a visible-light-driven photocatalyst for the degradation of amoxicillin [21]. MIL-53(Fe)-reduced graphene oxide (M53-RGO) nanocomposites have been successfully fabricated by a facile and efficient electrostatic self-assembly strategy for improving the photocatalytic reduction of Cr(VI) [22]. Inspired by those good results, and for further investigate the synergistic effect between MOFs and GO, we have tried to explore other GO-based MOFs composites as highly efficient photocatalysts [23,24].

Up to date, there are several Fe-based MOFs have been successfully prepared, such as MIL-100 [25], MIL-101 [26], MIL-53 [27], MIL–88 B [28] and MIL-88A [29]. While most of the Fe-based MOFs are synthesized using N, N-dimethylformamide (DMF) as a solvent, if the solvent is not completely removed during the synthesis, DMF will cause secondary contamination in the application process. Thus, a DMF-free Fe-based MOF could be an appropriate MOF material for the design of MOFs/GO heterojunction structures. To the end, MIL-88A(Fe) is selected in this work because it can be prepared by the coordination of fumaric acid and $FeCl_3 \cdot 6H_2O$ just in the water. We introduced graphene oxide into the MIL-88A(Fe) to form MOFs/GO heterogeneous structures for enhancing the photocatalytic activity of the MOFs. The MIL-88A(Fe)/GO-H_2O_2 systems exhibit better photocatalytic efficiency for the removal of Rhodamine B (RhB) than that of pure MIL-88A(Fe)-H_2O_2 under visible light irradiation. The introduction of H_2O_2 as electron acceptor can significantly improve the photocatalytic RhB removal of MIL-88A(Fe). Meanwhile, GO played a significant part in the photocatalytic reaction as well. Moreover, the MIL-88A(Fe)/GO photocatalyst exhibits a high stability and reusability in aqueous solution.

2. Experimental

In this study, all the chemical reagents used were purchased from Sinopharm Chemical Reagent Co., Ltd., (China). And all chemicals and reagents in this research were of commercially available analytical grade and used without any further purification.

2.1. Preparation of photocatalysts

2.1.1. Synthesis of graphene oxide nanoribbons

Graphite oxide (GO) was prepared by the Hummers method with some modifications [30]. In a flask, 6.0 g Graphite was added into 140 mL of H_2SO_4 (98 wt%) and stirred in an ice bath for 10 min. 3.0 g sodium nitrate ($NaNO_3$) and 18.0 g potassium permanganate ($KMnO_4$)

were mixed into the flask and the reaction mixture was stirred at 20 °C for 3 h. Then the reaction temperature was raised to 35 °C. After 4 h, the reaction mixture was slowly diluted with 300 mL of water, and the reaction temperature rapidly rose to 95 °C. After another 2 hours, 40 mL of H_2O_2 (30 wt%) and 600 mL of water were dripped into the reaction system. The sample was collected by centrifugation. The precipitation was washed with 10% HCl, and then dialyzed for 7 days with water. After centrifugation, the particle was GO.

2.1.2. Preparation of MIL-88A(Fe)

MIL-88A(Fe) was prepared according to the literature with some modifications [31]. In a specific procedure, $FeCl_3 \cdot 6H_2O$ (1.352 g) and $C_4H_4O_4$ (0.580 g) were mixed into 25 mL ultrapure water and then stirred by magnetic force till it turned into homogeneous solution, then it was put into autoclave and heated at 65 °C for 12 h. After cooling to room temperature, the sample was collected by centrifugation and dried under vacuum at 65 °C.

2.1.3. Synthesis of M88/GO nanocomposites

Scheme 1 shows a schematic diagram of the synthesis procedure. The MIL-88A(Fe)/Graphene oxide hybrids were prepared by a feasible hydrothermal reaction by controlling the mass ratios of MIL-88A(Fe) vs Graphene oxide. Firstly, a scheduled amount of GO powder was dissolved into 10 mL ultrapure water under ultrasonic conditions. Then $FeCl_3 \cdot 6H_2O$ (1.352 g) and $C_4H_4O_4$ (0.580 g) were added into 25 mL ultrapure water and stirred continuously, when it become homogeneous mixture, the GO solution was slowly dropped into the above solution and stirred vigorously for 2 h. Then it was put into hydrothermal conditions in an autoclave for 12 h at 65 °C. And the other procedure of the above solution remaining was the same as that of MIL-88A(Fe). The final products were labeled as M88/GO-1, M88/GO-5, M88/GO-9, and M88/GO-11 (the abbreviated numbers in the name represent the weight content of the GO for 1%, 5% , 9% , 11%).

2.2. Materials Characterization

The XRD patterns were performed using a XRD diffractometer (Bruker D8 ADVANCE) that was run at 40 mA and 40 kV using Cu Kα radiation. The Fourier transform infrared (FT-IR) spectroscopy was conducted on Smart Omni-Transmission FTIR Spectrometric Analyzer. The morphology of the samples was obtained from a JEOL JEM-2010F transmission electron microscope (TEM) operating at 200 kV and a Hitachi FESEM-4800 scanning electronic microscopy (SEM). X-ray photoelectron spectroscopy (XPS) surveys were obtained by using a ESCALAB 250Xi system. UV–vis diffuse reflectance spectra (UV–vis DRS) were recorded by a UV-2600 UV–vis spectrometer and $BaSO_4$ was applied as a reflectance standard in the experiment. The photoluminescence (PL) spectra was conducted at an excitation wavelength

of 320 nm (Hitachi F-7000).

2.3. Evaluation of photocatalytic activity

The photocatalytic degradation of RhB aqueous solution was conducted over M88A/GO composites under visible light irradiation. A 500W Xe lamp (PLS-SXE 500, CEAULIGHT Beijing) with a 420 nm cutoff filter (420 nm < λ < 760 nm) was used as the light source. Typically, 20 mg of photocatalyst sample and 50 mL RhB aqueous solution (10 ppm) were mixed into the photoreactor. In the dark condition, the solution should magnetically stirred for 60 min to achieve the adsorption-desorption equilibrium. Then a certain amount of H_2O_2 was put into the mixture solution, with the Xe lamp being switched on simultaneously. At scheduled time intervals, 2 mL of sample solution was taken from the reactor and separated by centrifugation. The concentration of RhB remained in the supernatant solution was calibrated at its maximum absorption wavelength of 554 nm by using a Xin Mao 723 PCS UV–vis spectrophotometer.

2.4. Electrochemical Measurements

The photocurrent measurements, electrochemical impedance spectroscopy (EIS) and Mott-Schottky analysis were carried out on an electrochemical workstation (CHI660C Apparatuses). The preparation of photoelectrodes was referred to the approach stated by Zhao et al. [32]. For the fabrication of the MOF electrodes, 20 mg the hybrids were spread in 20 mL chitosan solution and ultrasonicated for 30 min. Then, a certain amount of the mixture was put evenly on the conductive side of the ITO glass and dried in an oven at 60 °C for 12 h. In a standard three-electrode system, the catalyst composite was used as the working electrodes, a Pt foil and a normal hydrogen electrode (NHE) were used as the counter electrode and the reference electrode, respectively. Amperometric I-t curves were determined at a 0.8 V bias voltage potential (vs NHE) and a 500 W Xe arc lamp with a 420 nm cutoff filter was employed as a light source. The Mott-Schottky measurements were implemented with impedance-potential model to measure the band positions of the MIL-88A(Fe) and M88A/GO-9. EIS tests were conducted under dark circumstance at open circuit potential at the range of frequency between 10^5 and 10^{-2} Hz. All of the experiments were carried out in 0.5 M Na_2SO_4 solution.

3. Results and discussion

3.1. Characterizations

The crystallinity of GO, MIL-88A(Fe) and M88/GO composites are determined by X-ray diffraction (XRD) and the results are shown in Fig. 1. GO displays a sharp and intense diffraction peak at $2\theta = 11.59°$, corresponding to an interlayer spacing of 0.74 nm according to Bragg's Law [33]. The positions of all peaks of the pristine MIL-88A(Fe) sample are in good agreement with the previous MIL-88A(Fe), which confirms that the sample is successfully synthesized [31]. Interestingly, for the hybrid composites, when a small amount of GO is doped in MIL-88A(Fe) nanocomposite (M88/GO-1 and M88/GO-5), the main peak from MIL-88A(Fe) is preserved except some other peaks induced from GO (2 Theta ∼ 11.4 and 12.2°). However, while the doping content of GO increases to a certain amount (M88/GO-9 and M88/GO-11), most peaks from the component of MOF are disappeared except that only small intensity peaks are detected at approximately 10.7° and some new peaks produced in these hybrids. Some other MOF/GO hybrids also exist the similar changes of XRD patterns, such as MIL-100(Fe)/GO [34], MOF-5/GO [35], MOF-benzoic acid functionalized graphene [36]. These results are ascribed that the doping of GO changes the lattice structure of MOFs. The proper crystallization of the MIL-88A(Fe) may be prevented by the dispersed of GO on the surface of MIL-88A(Fe), so GO leads to change of lattice constitution of MIL-88A(Fe) [34–36].
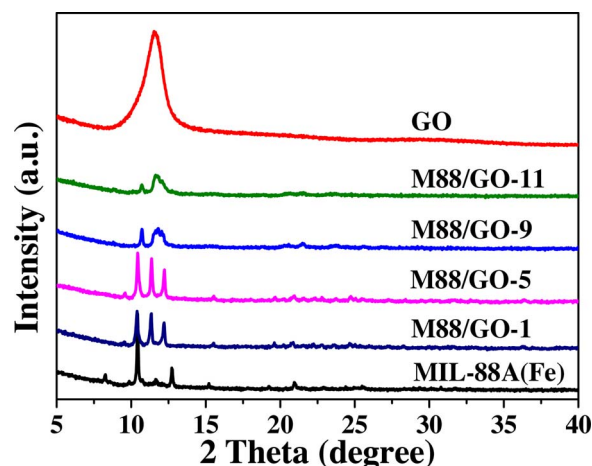

Fig. 1. XRD patterns of MIL-88A(Fe), GO and M88/GO nanocomposites.

The comparison of the FT-IR of the parent MIL-88A(Fe), GO and M88/GO composite samples are performed and shown in Fig. S1(a). The two intense peaks at 1396 and 1597 cm^{-1} are from the symmetric and asymmetric vibrations of the carboxyl group, respectively, while the wavenumber scope below 1300 cm^{-1} is associated with the out-of-plane vibrations of the same functionality [37]. Around 3000–3700 cm^{-1}, vibrations are detected from water molecules. From these results, one can find out that the FT-IR spectra of the M88/GO composites and MIL sample are identical. These imply that graphene layers do not inhibit the constitution of the MIL-88A(Fe) unit and they simply influence the lattice structure of MOF (as indicated by XRD). The results of thermogravimetric analyses of MIL-88A(Fe) and the M88/GO nanocomposites in air are displayed in Fig. S1(b). The weight loss from 30 °C to 100 °C is related to the removal of physically adsorbed water. The main weight loss, between 290 °C and 380 °C, might refer to the breakdown of the organic ligand followed by the progressive reduction of the iron species from Fe_3O_4 to Fe_2O_3 and then FeO [38]. The MIL-88A(Fe) and the M88/GO composites have similar thermal stabilities.

The porous properties of the as-synthesized samples are performed by nitrogen physisorption method. Fig. 2 and Table 1 show the adsorption-desorption isotherms, pore size distributions and the full data. The N_2 adsorption/desorption isotherms observed over MIL-88A(Fe) and M88/GO-1 attributed to IV-type adsorption curve and The N_2 adsorption/desorption isotherms observed over M88/GO-5, 9, 11 could be ascribed to I-type adsorption curve. The specific surface area of GO, MIL-88A(Fe) and M88/GO-1, 5, 9, 11 are measured to be 12.8, 15.9, 80.6, 239.9, 408.9 and 240.5 $m^2 g^{-1}$, respectively. Since the addition of GO affects the crystallization process of MOF, the specific surface areas are increased with the increase of GO amounts until the amount of GO is 9 wt% and a typical coexistence of micropores and mesopores can be revealed in M88/GO-5, 9, 11 [21,35,39–41]. The enhanced surface area may be attributed to the emerging micropores created at the interface between the GO and MIL-88A(Fe) components, as evidenced by the N_2 isotherm measured on M88/GO-9 and the corresponding PSD plot. However, when further increased the content of GO, the specific surface areas of M88/GO-11 is smaller than M88/GO-9, which demonstrates the number of functional groups on GO surface occupies the number of reactive sites on MIL blocks [39]. Additional explanation can be ascribed to that higher GO content, to some degree, caused distortion in the structure of MOFs due to the strong dispersive forces of GO [39].

To testify the GO loading onto MIL-88A, we examined the pure MIL-88A(Fe) and M88/GO-9 sample by SEM and TEM. As a comparison, the SEM images of M88/GO with different amount of GO were also conducted (see Fig. S2). As shown in Fig. 3, the original MIL-88A(Fe) shows well-crystallized needle-shaped microrods with an average size of 1–8 μm in length and 200–1000 nm in diameter (Fig. 3(a) and (b)).
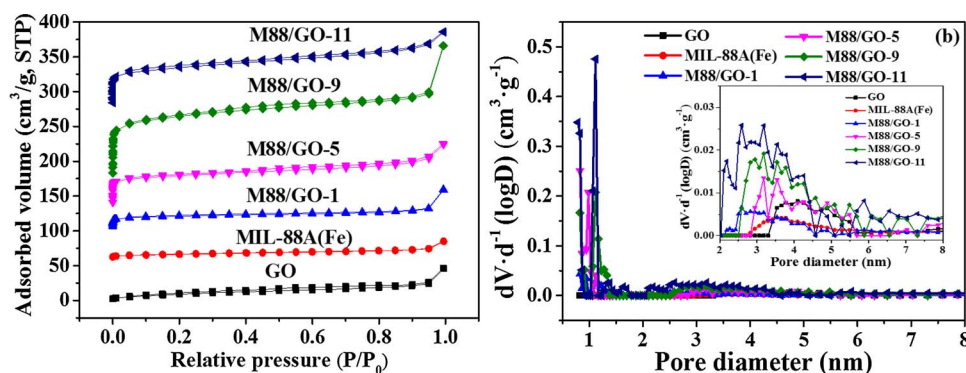
Fig. 2. N_2 adsorption-desorption isotherms (a) and pore size distribution (b) of GO, MIL-88A(Fe) and M88/GO composites.

Table 1
Physicochemical parameters of the photocatalysts.

Samples	BET ($m^2 g^{-1}$)	V (cc g^{-1})	D (nm)
GO	12.8	0.031	4.11
MIL-88A(Fe)	15.9	0.036	3.76
M88/GO-1	80.6	0.093	2.59-3.19
M88/GO-5	239.9	0.184	0.98/3.17-3.55
M88/GO-9	408.9	0.360	1.12/2.60-3.21
M88/GO-11	240.5	0.197	1.12/2.95-3.17

From the SEM of images of M88/GO-9 (Fig. 3(c) and (d)), it can be observed that the nanocomposite remains the needle-shaped structure of MIL-88A(Fe) with an average size of 1–3 μm in length and 200–500 nm in diameter, and GO distributes evenly and tightly on the surface of the nanocomposite. This phenomenon of the sizes of the MIL-88A(Fe) crystals in the M88/GO-9 composite are smaller than those of the parental ones, which indicates that the introduction of GO in the composite has certain influences on the building of the MIL-88A(Fe) crystals during the synthesis process, which is consistent with the reported results in the literature [21]. The TEM image shown in Fig. 3((e) and (f)) further confirms this phenomenon, where the silk-like GO nanolayers closely wrap on the MIL-88A(Fe) microrod, leading to intimate contact between MIL-88A(Fe) microrod and GO nanosheet. Of note, such long-ranged contact is favorable to form sufficient interface to mediate charge transfer during photocatalytic process.

XPS analysis was employed to determine the chemical states and bonding configuring of the M88/GO-9. In Fig. 4(a), the XPS survey spectrum illustrated that M88/GO-9 was mainly consisted of Fe, C and O elements. In the high-resolution XPS spectrum (Fig. 4(b)) of C 1s, the appearance of three peaks at 288.8, 286.9 and 284.8 eV could be respectively ascribed to carboxylic bonds, C=O and benzoic rings of GO [42,43]. Fig. 4(c) displays the high-resolution XPS spectra of O 1s, matched by three peaks at binding energies of 533 eV, 532.2 eV and 531.45 eV, which are ascribed to C-O, the oxygen components on the carboxylate groups of the $C_4H_4O_4$ and the Fe-O bonds of M88/GO-9, respectively[17,44]. For the high resolution XPS spectrum of Fe 2p (Fig. 4(d)), the binding energy peak at 711.8 eV is assigned to the Fe $2p_{3/2}$, and the peak at 725.5 eV is ascribed to the Fe $2p_{1/2}$ [43], and the peak distance was about 13.7 eV. These characteristics were highly similar to those reported reference Fe_2O_3 [45]. The two peaks with a satellite signal at 718 eV are feature of Fe(III) in GO-M88A-9 structure [46]. Furthermore, in comparison with the Fe(III) typical peaks of the MIL-88A(Fe) (Fig. 4(d)), the XPS characteristic of the Fe 2p doublet for M88/GO-9 shifts to the lower binding energy (Fig. 4(d)). Which can be attributed to an intimate interfacial contact between MOFs and GO in the M88/GO-9 hybrids [22]. Thus, the results are all consistent with that of the XRD and TEM, which further verify the M88/GO-9 has been successfully prepared by a simple one-pot hydrothermal reaction.

The absorbance properties of the MIL-88A(Fe) and M88/GO composites were probed by UV–vis DRS. As shown in Fig. 5(a), all samples display the significant light absorption at the range of 200–600 nm. For the pure MIL-88A(Fe), the signature absorption was detected at about 250 nm, which should be ascribed to the absorption resulted from ligand-to-metal charge transfer (LMCT) of O(II) to Fe(III) [47]. Moreover, the bands at the range of 300–500 nm can be assigned to the spin-allowed d-d transition ($[^6A_{1g} = > {}^4A_{1g} + {}^4E_g$ (G)]) of Fe (III) in MOFs [48,49]. It could be seen that the absorption edge of M88/GO composites is similar to that of pure MIL-88A(Fe), but the optical absorption intensity is increased obviously in the visible region range after the introduction of appropriate amount of GO, which possesses intensive absorption in the visible light region [50]. Correspondingly, the color change of MIL-88A(Fe) is observed; the yellow-orange color of MIL-88A(Fe) turns to dark orange and even becomes dark when the relatively large amount of GO is introduced (inset in Fig. 5(a)), which is in agreement with previous observations in other GO-based composites [51,52].

The band gap energy (E_g) of MIL-88A(Fe) and M88/GO-9 was estimated according to the intercept of the tangents to the plots of $(\alpha h\nu)^2$ vs. photo energy, as shown in Fig. 5(b). The band gaps of MIL-88A(Fe) and M88/GO-9 are 2.58 and 2.19 eV, respectively, illustrating that the introduction of graphene oxide narrows the band gaps. It is notable that the M88/GO-9 sample displays more strong absorption in comparison with pure MIL-88A(Fe) and shifts to long wavelength, while the yellow-orange colour of MIL-88A(Fe) sample turns to light black (see Fig. 5(a)). Those results illustrate that the visible light response of the samples is enhanced, which may improve the photocatalytic efficiency by producing more photogenerated carriers.

3.2. Photocatalytic properties

In this study, the photocatalytic performance of the M88/GO composites for the decolorization of RhB under visible light could be evaluated by UV–vis absorption spectra. As showed in Fig. 6(a), during the dark period, RhB is mainly removed from the solution by the adsorption of MIL-88A(Fe), M88/GO-1, 5, 9, 11. These samples reached adsorption-desorption equilibrium in 40–60 minutes and the adsorption percentage at 60 min was 7.8%, 10%, 19%, 26% and 22%, respectively, which is consistent with BET analysis. Upon visible light irradiation, in the absence of photocatalysts, no variation of RhB is observed with 80 min, illustrating the stability of RhB in the visible light irradiation. After adding a small amount of H_2O_2 to the RhB solution, the removal efficiency of RhB increases to 14% under visible light, which could be attributed to the photolysis of H_2O_2 to form reactive ·OH (H_2O_2 + visible light → ·OH + OH^-). Since the additive amount of H_2O_2 is very important in the Fenton-like reaction, we carried out the experiments about different additive amount of H_2O_2 (see Fig. S3), which indicated that the optimum dosage of H_2O_2 is 20 mM. As a comparison, MIL-88A(Fe) could degrade about 45% of RhB with H_2O_2, which was ascribed to the activation of H_2O_2 to form reactive ·OH by iron-based MIL-88A(Fe) and reactive charge carriers produced from Fe-O clusters in the MIL-88A(Fe). However, the removal rate of RhB was
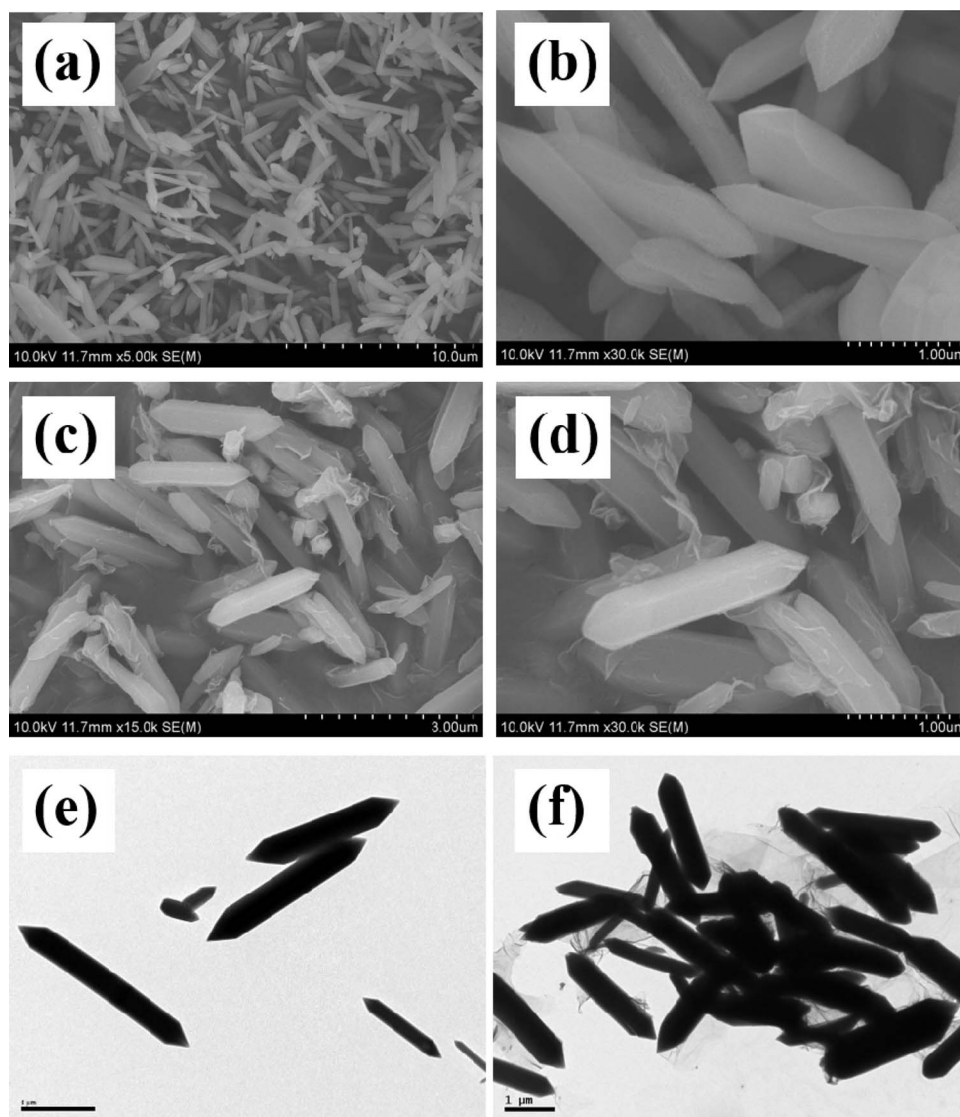
Fig. 3. SEM images of MIL-88A(Fe) (a, b) and M88/GO-9 (c, d); TEM images of MIL-88A(Fe) (e) and M88/GO-9 (f).

unsatisfactory, which might be attributed to the poor migration and separation of photoinduced charge carriers [25]. Interestingly, the photocatalytic activity could be boosted by the doping of graphene oxide on the surface of MIL-88A(Fe), and RhB was almost completely degraded within 80 min in the M88/GO-9/H$_2$O$_2$/Vis system. The performance was increased with the graphene oxide doping increased to 9 wt%. We also investigated the photocatalytic performance over GO, MOF and GO-M88A-9 before and after the addition of H$_2$O$_2$ (Fig. S4).

It is important to obtain the optimum doping amount of GO so as to achieve the best synergistic effect between GO and MIL-88A(Fe) for degradation of RhB. As for M88/GO nanocomposites, after the addition of a small amount of GO (1%), the degradation ratio is significantly increased to 88%. Interestingly, when continue to increase the content of GO to 9%, the optimal photocatalytic efficiency is achieved. After 80 min of visible light irradiation, RhB can be almost completely decolorized. However, when the content of GO reaches to 11%, the photocatalytic activity gradually decreases. The phenomenon is similar to that in other reported literatures [53,54]. Regarding the M88/GO, the high content of GO results in the decreased photocatalytic activity may because that some of the active sites on the MIL-88A(Fe) surface has been shielded by GO [55]. The kinetics curve of RhB degradation is in accordance with the pseudo-first-order process by linear transformation ln (C$_0$/C) = kt [48] (Fig. 6(b) and (c)). Under the same circumstances, the pseudo-first order reaction kinetics (k) of RhB removal over the M88/GO-9 is 0.0645, which is 8.4 times higher than that of pure MIL-88A(Fe) (k = 0.0077), and 3.4, 2.1 and 1.7 times higher than that of M88/GO-1, 5, 11, respectively. It also can be seen in Fig. 6(d) that M88/GO-9 displays excellent degradation effect in pH = 1 ∼ 9, verifying that it is a material being efficiently used in a wide range of pH. And we carried out the XRD patterns of M88/GO-9 composites before and after the photocatalytic experiments at pH = 11. From the XRD patterns (see Fig. S5), we can conclude that M88/GO-9 may be partially decomposed. Moreover, the degradation rate of phenol, methyl blue and methyl orange over M88/GO-9 could reach to 95.8%, 92.0% and 93.2%, respectively (see Fig. S6).

3.3. Reusability and stability of M88/GO nanocomposite

To assess the possibility of the catalyst in practical applications, the reusability and stability of M88/GO-9 have also been investigated. As shown in Fig. 7, photocatalytic activity of M88/GO-9 does not obviously decrease after five recycles for the degradation of RhB, suggesting that the M88/GO-9 photocatalyst possesses high stability and can be used for repeated treatment of RhB dye. Moreover, the XRD diffraction patterns (Fig. S7(a)) and FT-IR spectra (Fig. S7(b)) of M88/GO-9 before and after the reaction indicate that the crystal structure and surface active groups of M88/GO-9 have no obvious change even after the five cycles of the reaction. In summary, it demonstrates that
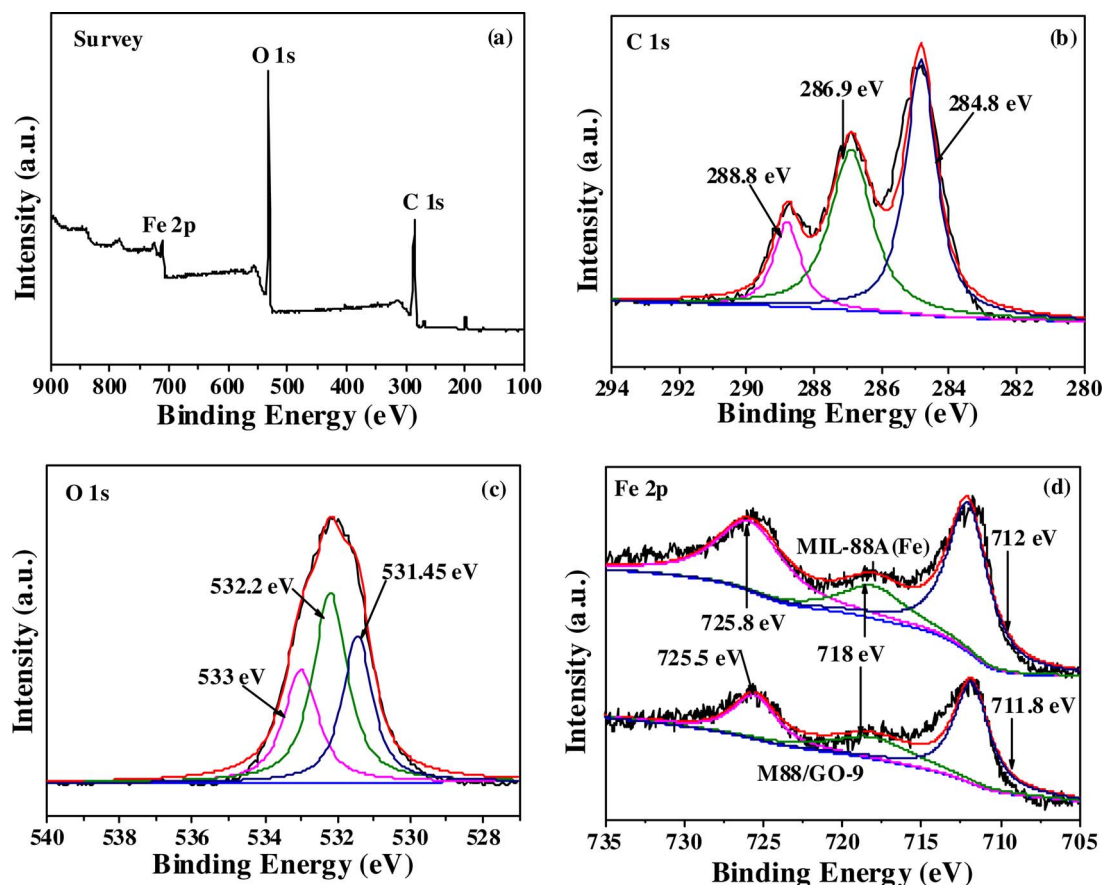
Fig. 4. XPS spectra of M88/GO-9 compared with the parent MIL-88A(Fe): (a) survey, (b) C 1s, (c) O 1s, and (d) Fe 2p.

the M88/GO-9 composite is stable in the photocatalytic process and has potential value for practical application.

3.4. Possible photocatalytic mechanism

In order to clarify the photocatalytic mechanism of the M88/GO-9/ H_2O_2 system, the quenchers of p-benzoquinone (BQ, $\cdot O_2^-$ scavenger), $AgNO_3$ (an electron scavenger), isopropyl alcohol (IPA, a $\cdot OH$ scavenger) and EDTA-2Na (h^+ scavenger) are used to trap the major active species involved in the removal of RhB under visible light irradiation [56–58]. As shown in Fig. 8, the photocatalytic degradation of RhB is obviously inhibited after the addition of BQ, $AgNO_3$ and IPA, indicating that $\cdot O_2^-$, e^- and $\cdot OH$ play the more important part as the relevant oxidative species in the reaction.

The photoluminescence (PL) emission is produced by the recombination of photogenerated electrons and holes, so that PL technique can be applied to illustrate the effectiveness of charge carrier separation, migration and transfer, as well as investigated the lifetime of charge carriers in the composites [59,60]. Fig. 9(a) shows the PL spectra of MIL-88A(Fe) and GO-M88A-9 with an excitation wavelength of 320 nm [61]. It can also be found that the PL intensity of the MIL-88A(Fe) is much stronger than that of M88/GO-9 indicating that the M88/GO-9 has the longer lifetime of electron-hole pairs. Combined with the morphology analysis of the M88/GO-9 sample, it was acknowledged that the surface heterojunction structure between the Fe-MOFs and the GO could enhance the separation of the photon-induced carrier, namely, GO can serve as a good electrons acceptor in the photocatalytic reaction, and as a result, the migration of the electron-hole is enhanced. This state of the long-lived electron-hole can make the M88/GO-9 have an enhanced photocatalytic effect, which is consistent with the results of the photocatalytic performance.

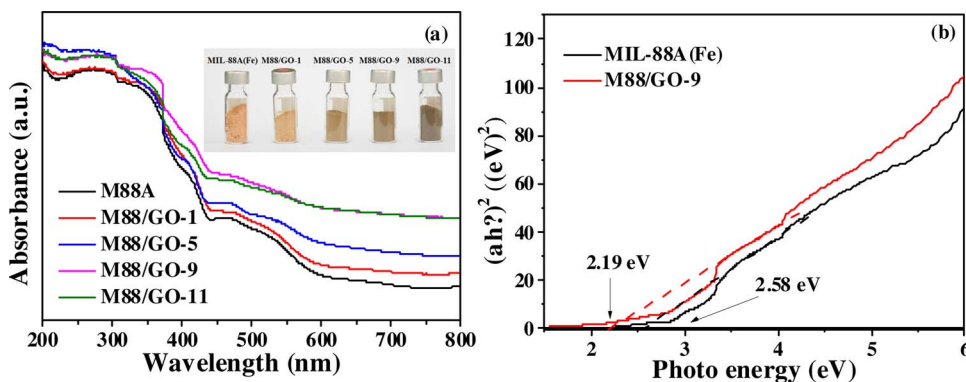From the above results, it can be believed that the introduction of

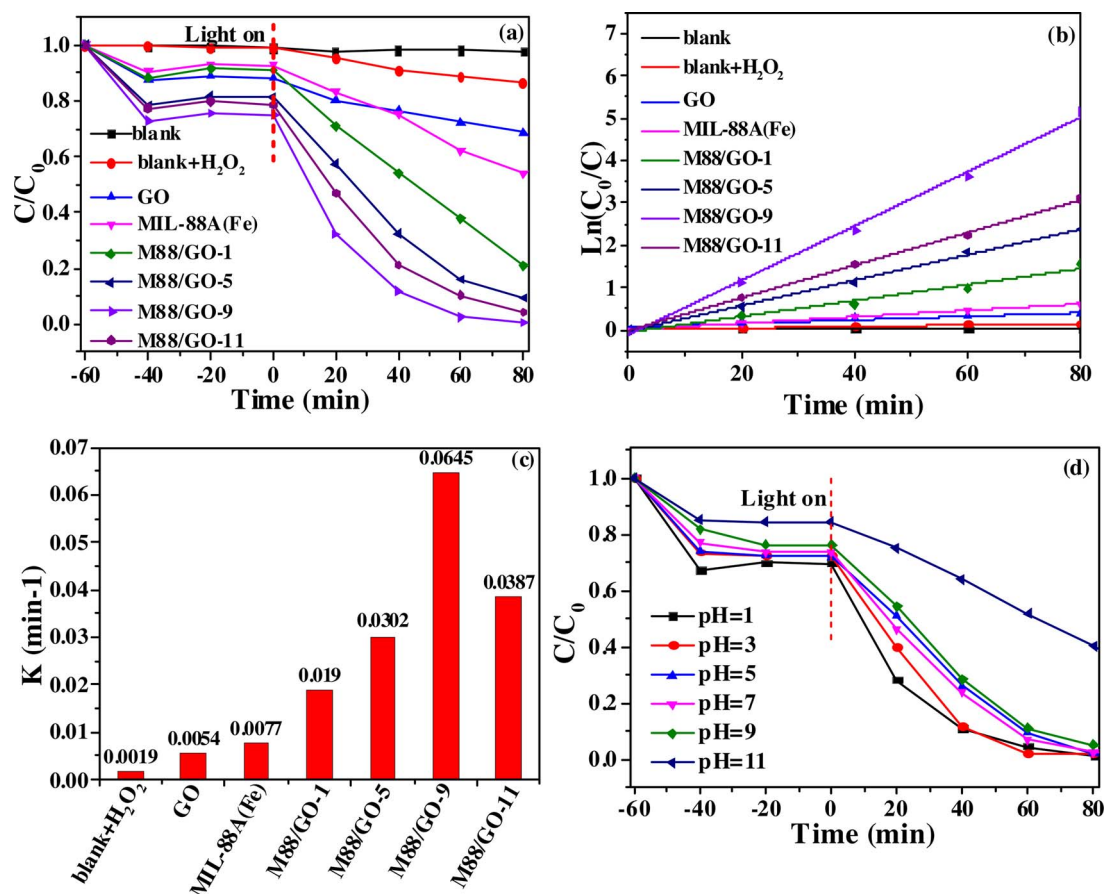**Fig. 5.** UV–vis DRS spectra (a) and the band gaps (b) of MIL-88A(Fe) and M88/GO nanocomposites.

Fig. 6. Photocatalytic degradation curves (a) and the apparent reaction rate constants (k) of RhB (b, c) using different photocatalysts after 80 min of visible light irradiation; Effect of initial pH on the degradation of RhB. Experimental conditions: RhB, 10 mg L^{-1}; H$_2$O$_2$, 20 mM; and Phocatalyst, 0.4 g L^{-1}.
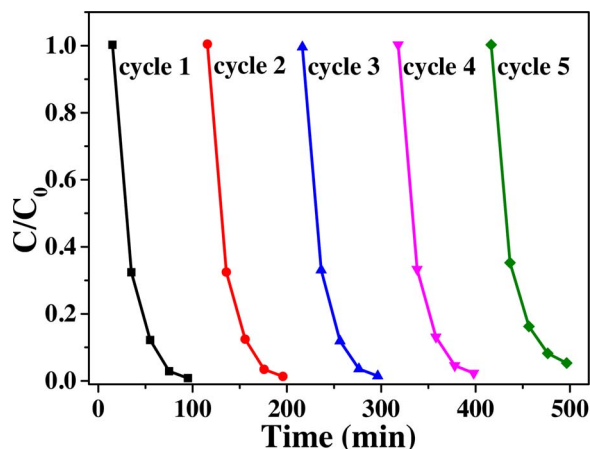

Fig. 7. The reusability of M88/GO-9 nanocomposite for the photodegradation of RhB.

Fig. 8. Effect of different scavengers on the photodegradation of RhB by M88/GO-9 nanocomposite under visible-light irradiation. Experimental conditions: RhB, 10 mg L^{-1}; H$_2$O$_2$, 20 mM; Phocatalyst, 0.4 g L^{-1} and initial pH 7.

GO affect the charge transfer behaviors of M88/GO-9 composites and reduce recombination rate of the electron and hole. Thus, the photo-induced charge separation and transfer properties were estimated by the EIS and the photocurrent measurements. Fig. 9(b) shows the experimental Nyquist impedance plots of MIL-88A (Fe) and M88/GO-9 composites in 0.5 M Na$_2$SO$_4$ solution under dark condition. Compared with parent MIL-88A(Fe), the radius of Nyquist arc of M88/GO-9 gradually decreases, which indicates that the GO loading is beneficial to improve the charge transfer efficiency in MIL-88A(Fe) because GO has superior electrical conductivity. The photocurrent-time curves for the MIL-88A(Fe) and M88/GO-9 are displayed in Fig. 10. It can be observed that, the photocurrent response of M88/GO-9 under visible light
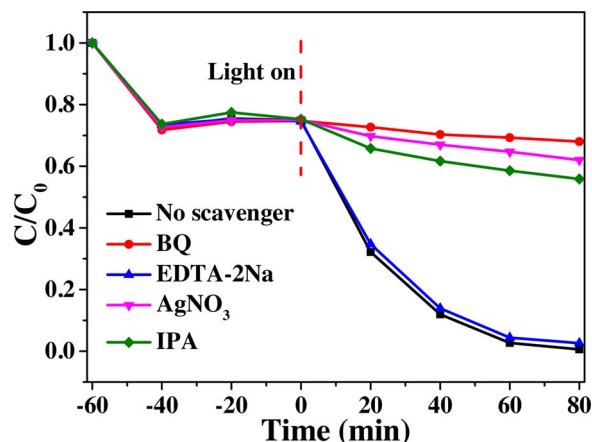
irradiation increases with respect to the MIL-88A(Fe), showing that M88/GO-9 possesses a more efficient separation efficiency of photo-excited electron-hole pairs and a rapider interfacial charge transfer. And the photocurrent is recyclable and stable. The results can be implied to the fact that the two-dimensional ultrathin structure is favorable for electron transfer and the direct recombination of photogenerated charge may be suppressed by the electrophilic groups (C-O, C=O and COOH).

In order to further understand the reasons for the increased photocatalytic effect of RhB degradation by M88/GO-9, Mott-Schottky
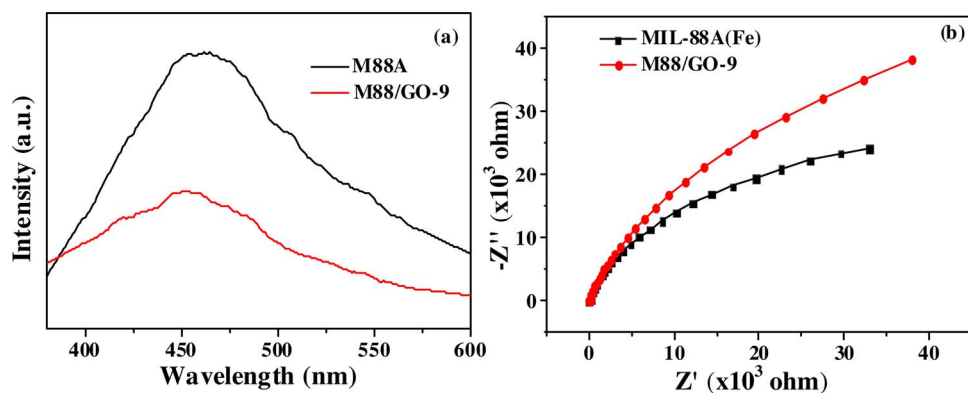
Fig. 9. PL spectra (a) and EIS Nyquist impedance plots (b) of MIL-88A(Fe) and M88/GO-9.
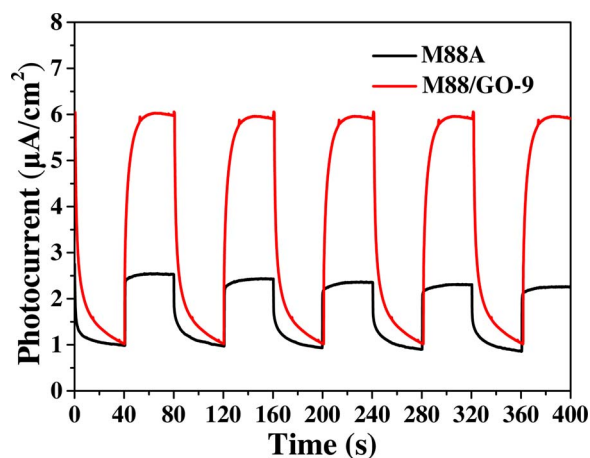

Fig. 10. Transient photocurrent responses of M88A and M88/GO-9 nanocomposite.

measurement was carried out to determine the band structure of M88/GO-9. Mott-Schottky measurement of the M88/GO-9 catalyst is performed in the dark at a frequency of 1 kHz. As shown in Fig. 11(a), the position slope of the plot reveals that M88/GO-9 is an n-type semiconductor characteristic. The flat-band potential of M88/GO-9 derived from Mott-Schottky plot is about -0.60 V versus NHE. For n-type semiconductors, the conduction-band potential was 0.1 V lower than the flat-band potential [62]. As illustrated in Fig. 11(b), the conduction band potential (E_{CB}) of M88/GO-9 is extrapolated to be about -0.70 V versus NHE , which is lower than the potential of $O_2/\cdot O_2^-$ (0.13 eV) [63], so $\cdot O_2^-$ radical has contribution to the degradation process. Combined with the band gap energy calculated by UV–vis DRS spectra, the valence-band potential of M88/GO-9 is calculated to be 1.49 V versus NHE, being lower than the redox potential of $\cdot OH/OH^-$ (2.38 V versus NHE) and thus indicating that M88/GO-9 is unable to produce $\cdot OH$ radicals by oxidize OH^- through h^+ [17,64]. On the basis of above results, it is reasonably expected that produced more large amount of $\cdot$

OH radicals in M88/GO-H_2O_2-Vis system would be derived from the reduction of H_2O_2 by photogenerated electron ($H_2O_2 + e_{CB}^- \rightarrow OH^- + \cdot OH$) [65–67] , which should be the origin of the synergistic effect existed in the H_2O_2-containing catalytic system. Notably, the redox potential of RhB is about 1.43 V vs. NHE, which is significantly lower than VB level of MIL-88A(Fe) (see Fig. S8, $VB_{MIL-88A(Fe)} = 2.13$ V) [68], indicating that the photogenerated holes on the VB of MIL-88A(Fe) can directly oxidize the RhB.

In terms of the above analysis, a possible photocatalytic mechanism of M88/GO-9-H_2O_2 system is proposed and depicted in Fig. 12. Under visible light irradiation, M88/GO-9 can be excited to generate photogenerated electrons (e^-) and holes (h^+) in the conduction and valence band (Eqs. (1)). On the one hand, the photogenerated holes with strong oxidation capacity can oxidize the RhB directly. Meanwhile, due to the existence of ultrathin GO sheets, the photoexcited electrons can migrate to the GO, which improves the separation of photoinduced electron-hole pairs effectively and in the presence of hydrogen peroxide, the electrons in the CB can be trapped by H_2O_2 (Eqs. (2)); At the same time, the highly active specie $\cdot O_2^-$ radicals are produced on the surface of M88/GO-9 (Eqs. (3)), which can further oxidize RhB [25,69,70]. On the other hand, the Fe(III)-O clusters on the surface of M88/GO-9 can catalyze the decomposition of H_2O_2 to produce $\cdot OH$ radicals by the Fenton-like reaction (Eqs. (4) and (5)) [68,71]. Moreover, the unique ultrathin 2D constitution of GO sheets permit the photocatalytic reactions to go on both on the surface of GO sheets and MIL-88A(Fe), which provides more catalytic centers and increases the activity sites. Accordingly, M88/GO-9 hybrids show enhanced photocatalytic efficiency in photocatalytic redox reactions.
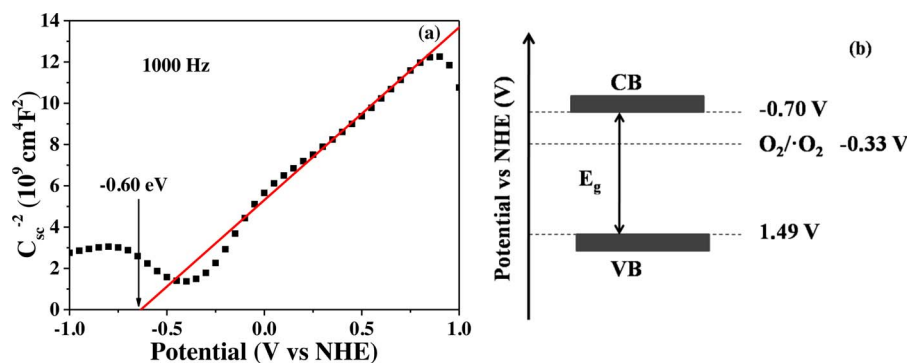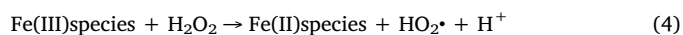
$$M88/GO-9 + h\nu \rightarrow h^+ + e^- \tag{1}$$

$$H_2O_2 + e^- \rightarrow \cdot OH + OH^- \tag{2}$$

$$e^- + O_2 \rightarrow \cdot O_2^- \tag{3}$$

$$Fe(III)species + H_2O_2 \rightarrow Fe(II)species + HO_2\cdot + H^+ \tag{4}$$

$$Fe(II)species + H_2O_2 \rightarrow Fe(III)species + \cdot OH + OH^- \tag{5}$$

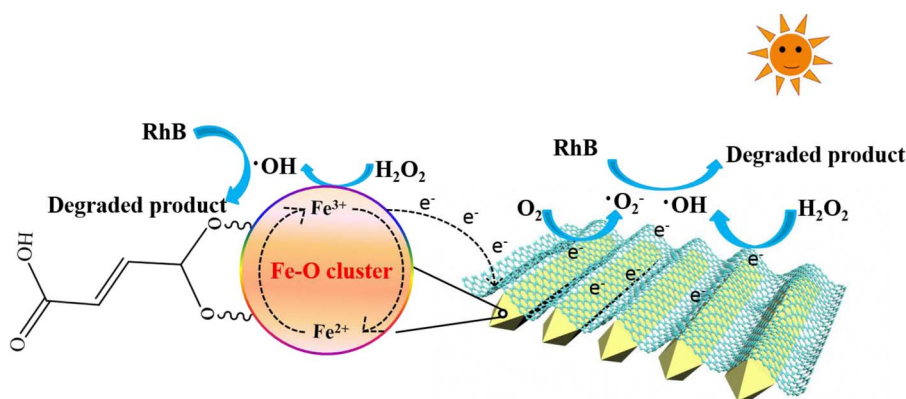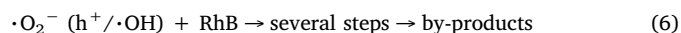**Fig. 11.** Mott-Schottky plots (a) and estimated energy level diagram (b) of the M88/GO-9.

Fig. 12. A schematic illustration of oxidation of RhB over M88/GO-9 nanocomposite under visible light irradiation.

$$\cdot O_2^- \ (h^+/\cdot OH) \ + \ RhB \rightarrow several \ steps \rightarrow by\text{-}products \tag{6}$$

4. Conclusions

In summary, the highly efficient visible light photocatalysts based on the GO hybridized MIL-88A(Fe) microrods have been rationally designed and fabricated by a facile one-pot solvothermal process. The MIL-88(Fe)/GO-H_2O_2 systems exhibit significantly higher photocatalytic activity toward degrading Rhodamine B (RhB) than that of bare MIL-88A(Fe)-H_2O_2 under visible light irradiation. The introduced H_2O_2 could induce photosynergistic generation of more amounts of hydroxyl radicals to contribute to the improved photocatalytic activity. This work could open a new way for the exploration and utilization of MOF-based crystalline materials for environmental applications.

Acknowledgements

Appendix A. Supplementary data

Supplementary data associated with this article can be found, in the online version, at http://dx.doi.org/10.1016/j.apcatb.2017.09.020.

References

[1] Y. Gao, S. Li, Y. Li, L. Yao, H. Zhang, Appl. Catal. B: Environ. 202 (2017) 165–174.
[2] X.D. Zhang, H.X. Li, F.L. Hou, Y. Yang, H. Dong, N. Liu, Y.X. Wang, L.F. Cui, Appl. Surf. Sci. 411 (2017) 27–33.
[3] X. Li, Y. Pi, L. Wu, Q. Xia, J. Wu, Z. Li, J. Xiao, Appl. Catal. B: Environ. 202 (2017) 653–663.
[4] A.U. Czaja, N. Trukhan, U. Muller, Chem. Soc. Rev. 38 (2009) 1284–1293.
[5] W.Y. Huang, N. Liu, X.D. Zhang, M.H. Wu, L. Tang. Appl. Surf. Sci. 425 (2017) 107–116.
[6] L.J. Murray, M. Dinca, J.R. Long, Chem. Soc. Rev. 38 (2009) 1294–1314.
[7] J. Lee, O.K. Farha, J. Roberts, K.A. Scheidt, S.T. Nguyen, J.T. Hupp, Chem. Soc. Rev. 38 (2009) 1450–1459.
[8] X.D. Zhang, F.L. Hou, Y. Yang, Y.X. Wang, N. Liu, D. Chen, Y.Q. Yang, Appl. Surf. Sci. 423 (2017) 771–779.
[9] Y. Bai, G.J. He, Y.G. Zhao, C.Y. Duan, D.B. Dang, Q.J. Meng, Chem. Commun (2006) 1530–1532.
[10] K.G.M. Laurier, E. Fron, P. Atienzar, K. Kennes, H. Garcia, M. Van der Auweraer, D.E. De Vos, J. Hofkens, M.B.J. Roeffaers, Phys. Chem. Chem. Phys. 16 (2014) 5044–5047.
[11] F. Xamena, A. Corma, H. Garcia, J. Phys Chem C. 111 (2007) 80–85.
[12] H. Yang, X.W. He, F. Wang, Y. Kang, J. Zhang, J. Mater. Chem. 22 (2012) 21849–21851.
[13] L.J. Shen, W.M. Wu, R.W. Liang, R. Lin, L. Wu, Nanoscale. 5 (2013) 9374–9382.
[14] L.J. Shen, S.J. Liang, W.M. Wu, R.W. Liang, L. Wu, Dalton Trans. 42 (2013) 13649–13657.
[15] H.J. Li, Y. Zhou, W.G. Tu, J.H. Ye, Z.G. Zou, Adv. Funct. Mater. 25 (2015) 998–1013.
[16] W. Zhu, P.J. Liu, S.N. Xiao, W.C. Wang, D.Q. Zhang, H.X. Li, Appl. Catal. B: Environ. 172 (2015) 46–51.
[17] C.H. Zhang, L.H. Ai, J. Jiang, Ind. Eng. Chem. Res. 54 (2015) 153–163.
[18] Z.F. Liu, Q. Liu, Y. Huang, Y.F. Ma, S.G. Yin, X.Y. Zhang, W. Sun, Y.S. Chen, Adv. Mater. 20 (2008) 3924–3931.
[19] L. Jia, D.H. Wang, Y.X. Huang, A.W. Xu, H.Q. Yu, J. Phys Chem C. 115 (2011) 11466–11473.
[20] Z. Yang, X. Xu, X. Liang, C. Lei, Y. Wei, P. He, B. Lv, H. Ma, Z. Lei, Appl. Catal. B: Environ. 198 (2016) 112–123.
[21] C. Yang, X. You, J. Cheng, H. Zheng, Y. Chen, Appl. Catal. B: Environ. 200 (2017) 673–680.
[22] R. Liang, L. Shen, F. Jing, N. Qin, L. Wu, ACS Appl. Mat. Interfaces. 7 (2015) 9507–9515.
[23] R. Lin, L.J. Shen, Z.Y. Ren, W.M. Wu, Y.X. Tan, H.R. Fu, J. Zhang, L. Wu, Chem. Commun. 50 (2014) 8533–8535.
[24] L.J. Shen, L.J. Huang, S.J. Liang, R.W. Liang, N. Qin, L. Wu, Rsc Adv. 4 (2014) 2546–2549.
[25] R. Liang, S. Luo, F. Jing, L. Shen, N. Qin, L. Wu, Appl. Catal. B: Environ. 176–177 (2015) 240–248.
[26] L. Chi, Q. Xu, X. Liang, J. Wang, X. Su, Small. 12 (2016) 1351–1358.
[27] Y. Zhang, G. Li, H. Lu, Q. Lv, Z. Sun, Rsc Adv. 4 (2014) 7594–7601.
[28] L. Shi, T. Wang, H. Zhang, K. Chang, X. Meng, H. Liu, J. Ye, Adv. Sci. 2 (2015) 1500006.
[29] C. Serre, F. Millange, S. Surble, G. Ferey, Angew. Chem. Int. Ed. 43 (2004) 6286–6289.
[30] J. Xu, L. Wang, Y.F. Zhu, Langmuir. 28 (2012) 8418–8425.
[31] W.T. Xu, L. Ma, F. Ke, F.M. Peng, G.S. Xu, Y.H. Shen, J.F. Zhu, L.G. Qiu, Y.P. Yuan, Dalton Trans. 43 (2014) 3792–3798.
[32] K. Zhao, X. Zhang, L. Zhang, Electrochem. Commun. 11 (2009) 612–615.
[33] M. Seredych, C. Petit, A.V. Tamashausky, T.J. Bandosz, Carbon 47 (2009) 445–456.
[34] C. Petit, T.J. Bandosz, Adv. Funct. Mater. 21 (2011) 2108–2117.
[35] C. Petit, T.J. Bandosz, Adv. Mater. 21 (2009) 4753–4761.
[36] M. Jahan, Q. Bao, J.X. Yang, K.P. Loh, J. Am. Chem. Soc. 132 (2010) 14487–14495.
[37] C. Mellot-Draznieks, C. Serre, S. Surble, N. Audebrand, G. Ferey, J. Am. Chem. Soc. 127 (2005) 16273–16278.
[38] S.C. Ndiela, B.H. Shanks, Ind. Eng. Chem. Res. 42 (2003) 2112–2121.
[39] Y. Chen, D. Lv, J. Wu, J. Xiao, H. Xi, Q. Xia, Z. Li, J. Chem Eng. 308 (2017) 1065–1072.
[40] S. Zhao, D. Chen, F. Wei, N. Chen, Z. Liang, Y. Luo, Ultrasonics sonochemistry 39 (2017) 845–852.
[41] C. Petit, J. Burress, T.J. Bandosz, Carbon 49 (2011) 563–572.
[42] D. Yang, A. Velamakanni, G. Bozoklu, S. Park, M. Stoller, R.D. Piner, S. Stankovich, I. Jung, D.A. Field, C.A. Ventrice, R.S. Ruoff, Carbon 47 (2009) 145–152.
[43] P.S. Johnson, P.L. Cook, X. Liu, W. Yang, Y. Bai, N.L. Abbott, F.J. Himpsel, J. Chem. Phys. 135 (2011) 044702–044711.
[44] S.K. Das, M.K. Bhunia, M.M. Seikh, S. Dutta, A. Bhaumik, Dalton Trans. 40 (2011) 2932–2939.
[45] C.M. Yu, L.L. Gou, X.H. Zhou, N. Bao, H.Y. Gu, Electrochim. Acta. 56 (2011) 9056–9063.
[46] R.W. Liang, F.F. Jing, L.J. Shen, N. Qin, L. Wu, J. Hazard. Mater. 287 (2015) 364–372.
[47] M. Alvaro, E. Carbonell, B. Ferrer, F. Xamena, H. Garcia, J. Chem Eur. 13 (2007) 5106–5112.
[48] G.T. Vuong, M.H. Pham, T.O. Do, Dalton Trans. 42 (2013) 550–557.
[49] G.T. Vuong, M.H. Pham, T.O. Do, Crystengcomm. 15 (2013) 9694–9703.
[50] X.J. Zou, Y.Y. Dong, X.D. Zhang, Y.B. Cui, Appl. Surf. Sci. 366 (2016) 173–180.
[51] S.W. Liu, C. Liu, W.G. Wang, B. Cheng, J.G. Yu, Nanoscale. 4 (2012) 3193–3200.
[52] Y.Y. Bu, Z.Y. Chen, W.B. Li, B.R. Hou, ACS Appl. Mat. Interfaces. 5 (2013) 12361–12368.
[53] Y.Q. Yang, H.X. Li, F.L. Hou, J.Y. Hu, X.D. Zhang, Y.X. Wang, Mater. Lett. 180 (2016) 97–100.
[54] S.Q. Liu, Z. Chen, N. Zhang, Z.R. Tang, Y.J. Xu, J. Phys Chem C. 117 (2013) 8251–8261.

[55] Y.H. Zhang, Z.R. Tang, X. Fu, Y.J. Xu, Acs Nano. 5 (2011) 7426–7435.
[56] S. Kumar, A. Baruah, S. Tonda, B. Kumar, V. Shanker, B. Sreedhar, Nanoscale. 6 (2014) 4830–4842.
[57] L. Shi, L. Liang, J. Ma, F.X. Wang, J.M. Sun, Catal. Sci. Technol. 4 (2014) 758–765.
[58] M.N. Khan, M. Al-Hinai, A. Al-Hinai, J. Dutta, Ceram. Int. 40 (2014) 8743–8752.
[59] S.C. Yan, Z.S. Li, Z.G. Zou, Langmuir. 26 (2010) 3894–3901.
[60] Y.C. Huang, W.J. Fan, B. Long, H.B. Li, F.Y. Zhao, Z.L. Liu, Y.X. Tong, H.B. Ji, Appl. Catal. B: Environ. 185 (2016) 68–76.
[61] Z.W. Tong, D. Yang, T.X. Xiao, Y. Tian, Z.Y. Jiang, J. Chem Eng, 260 (2015) 117–125.
[62] X.D. Zhang, Y.X. Wang, F.L. Hou, H.X. Li, Y. Yang, Y.Q. Yang, Y. Wang, Appl. Surf. Sci. 391 (2017) 476–483.
[63] C.N. Tang, E.Z. Liu, J. Fan, X.Y. Hu, Y.N. Ma, J. Wan, Rsc Adv. 5 (2015) 91979–91987.
[64] G.L. Zhou, H.Q. Sun, S.B. Wang, H.M. Ang, M.O. Tade, Sep. Purif. Technol. 80 (2011) 626–634.
[65] Y. Cui, Z. Ding, P. Liu, M. Antonietti, X. Fu, X. Wang, Phys. Chem. Chem. Phys. 14 (2012) 1455–1462.
[66] M. Ge, L. Liu, W. Chen, Z. Zhou, Crystengcomm. 14 (2012) 1038–1044.
[67] Y. Liu, Y. Zhu, J. Xu, X. Bai, R. Zong, Y. Zhu, Appl. Catal. B: Environ. 142 (2013) 561–567.
[68] L. Hu, G. Deng, W. Lu, S. Pang, X. Hu, Appl. Surf. Sci. 410 (2017) 401–413.
[69] M. Wen, K. Mori, Y. Kuwahara, T. An, H. Yamashita, Appl. Catal. B: Environ. 218 (2017) 555–569.
[70] M. Wen, Y. Cui, Y. Kuwahara, K. Mori, H. Yamashita, ACS Appl. Mat. Interfaces. 8 (2016) 21278–21284.
[71] L. Ai, C. Zhang, L. Li, J. Jiang, Appl. Catal. B: Environ. 148–149 (2014) 191–200.